INTERNATIONAL JOURNAL FOR NUMERICAL METHODS IN FLUIDS
Int. J. Numer. Meth. Fluids 2004; **44**:975–995 (DOI: 10.1002/fld.692)

Interfacial dynamics-based modelling of turbulent cavitating flows, Part-1: Model development and steady-state computations

Inanc Senocak[‡] and Wei Shyy[*,†]

Department of Mechanical and Aerospace Engineering, University of Florida, Gainesville, FL 32611, U.S.A.

SUMMARY

The merits of transport equation-based models are investigated by adopting an enhanced pressure-based method for turbulent cavitating flows. An analysis of the mass and normal-momentum conservation at a liquid–vapour interface is conducted in the context of homogeneous equilibrium flow theory, resulting in a new interfacial dynamics-based cavitation model. The model offers direct interpretation of the empirical parameters in the existing transport-equation-based models adopted in the literature. This and three existing cavitation models are evaluated for flows around an axisymmetric cylindrical body and a planar hydrofoil, and through a convergent–divergent nozzle. Although all models considered provide qualitatively comparable wall pressure distributions in agreement with the experimental data, quantitative differences are observed in the closure region of the cavity, due to different compressibility characteristics of each cavitation model. In particular, the baroclinic effect of the vorticity transport equation plays a noticeable role in the closure region of the cavity, and contributes to the highest level of turbulent kinetic energy there. Copyright © 2004 John Wiley & Sons, Ltd.

KEY WORDS: cavitation; turbulence; pressure-based method

1. INTRODUCTION

In liquid flows, cavitation generally occurs if the pressure in certain locations drops below the vapour pressure and consequently the negative pressures are relieved by the formation of gas-filled or gas- and vapour-filled cavities [1]. Cavitation can be observed in a wide variety of propulsion and power systems like pumps, nozzles, injectors, marine propellers,

---

[*] Correspondence to: Wei Shyy, Department of Mechanical and Aerospace Engineering, University of Florida, 231 Aerospace Building, P.O. Box 116250, Gainesville, FL 32611, U.S.A.

[†] E-mail: wss@mae.ufl.edu

[‡] Present address: Center for Turbulence Research, Stanford University, Building 500, Stanford, CA 94305-3035, U.S.A. E-mail: senocak@stanford.edu

Contract/grant sponsor: NASA URETI program
Contract/grant sponsor: U.S. Air Force

Received 29 March 2003
Revised 22 October 2003

hydrofoils and underwater bodies [2]. Such flows in most engineering systems are turbulent. The dynamics of the interface formed involves complex interactions between vapour and liquid phases. These interactions are not well understood in the closure region of the cavity where a distinct interface may not exist and the mean flow (in the sense of ensemble averaging) is unsteady.

The Navier–Stokes-based computations of turbulent cavitating flows have received growing attention due to advances in computational capabilities and physical modelling for these problems. In addition to high Reynolds number and multiphase nature of the flow, disparities between fluid properties of each phase, especially the density ratio, which is around 1000 for typical fluid machinery operating conditions, make such computations challenging. The inception and subsequent development of a cavity into other stages of cavitation, namely sheet, cloud, vortex and supercavitation, is driven by the phase change due to hydrodynamic pressure drop and bubble dynamics [2]. Owing to changes in fluid properties and physical mechanisms across the liquid–vapour boundaries, existing computational algorithms of single-phase, incompressible flow often experience severe convergence and stability problems for cavitating flows. To remedy this situation, improved numerical methods have been proposed. In the context of density-based methods, the artificial compressibility method has been applied with special attention given to the preconditioning technique [3–7]. Following the spirit of the well-established SIMPLE algorithm [8], a pressure-based method for turbulent cavitating flows has also been developed [9]. Both pressure- and density-based methods, adopting steady-state computations, have been successful in computing turbulent cavitating flows around axisymmetric bodies and hydrofoils with comparable accuracy.

A common approach in cavitation modelling is to use the homogeneous flow theory. In this theory, the mixture density concept is introduced and a single set of mass and momentum equations is solved. Different ideas have been proposed to generate the variable density field; a review of the published studies is given in Reference [10]. Some of the existing studies solve the energy equation and determine the density through suitable equations of state [4]. Since most cavitating flows are isothermal, arbitrary barotropic equations have been proposed to supplement the energy consideration [11, 12]. Another popular approach is the transport equation-based model (TEM) [3, 5–7, 9, 13]. In TEM, a transport equation for either mass or volume fraction, with appropriate source terms to regulate the mass transfer between phases, is solved. Different modelling concepts embodying varied source terms have been proposed by several researchers, as will be discussed in the next section. Growing experimental information can directly help assess the adequacy of the proposed physical models. For example, it has been shown that vorticity production is an important aspect of cavitating flows, especially in the closure region [14]. Specifically, this vorticity production is a consequence of the baroclinic generation term of vorticity equation, namely,

$$\nabla \frac{1}{\rho} \times \nabla P$$

Clearly, if an arbitrary barotropic equation $\rho = f(P)$ is used, then the gradients of density and pressure are always parallel; hence, the baroclinic torque is zero. This suggests that physical models which utilize a barotropic equation fail to capture an experimentally observed characteristic of cavitating flows. Likewise, solving an energy equation may also experience the same situation if the flow is essentially isothermal. However, in TEM approaches the density is a function of the transport process. Consequently, gradients of density and pressure are not necessarily parallel, suggesting that the TEM can accommodate the baroclinic vorticity generation. Based on this identification, the TEM approach is adopted in the present study.

Different modelling concepts have been introduced in the TEM with varied numerical treatments such as grid resolution and discretization accuracy. As a result, there is a lack of clear consensus on the capability and relative merits of these models. Three of these models, which have been employed in the literature, will be summarized in the coming sections. A common characteristic of these models is the use of empirical parameters to regulate the mass transfer process. Although these empirical parameters seem *ad hoc*, satisfactory results for different geometries and flow conditions have been obtained [15, 16]. The values of the empirical parameters are largely determined through numerical experimentation. Recently, Rajkumar *et al.* [16] have performed a systematic evaluation of the empirical parameters of a particular model [5] using the response surface methodology and design of experiments. Clearly, we can further the modelling capability by clarifying the key concepts and parameters involved via improved physical understanding. To realize this goal, better modelling capabilities are needed.

Hence, the goals of the present study are as follows:

- Develop a transport equation-based cavitation model, and address the empiricism in the existing cavitation models.
- Assess the predictive capability of transport equation-based cavitation models using well documented experimental information.
- Study the cavitating flow structure involving, in particular, vorticity dynamics and turbulence production.

In what follows, the governing equations and the numerical method are briefly presented first. Three transport equation-based cavitation models from the literature are summarized. Following this, an analysis of the mass and momentum conservation at a liquid–vapour phase change interface is conducted and a new interfacial dynamics-based cavitation model is developed. Based on the available experimental data in literature, the new cavitation model and three empirical cavitation models are evaluated for flow around an axisymmetric, hemispherical projectile and an NACA66MOD hydrofoil. The new model is further employed to study the flow structure in a convergent–divergent nozzle.

2. GOVERNING EQUATIONS AND NUMERICAL METHOD

The set of governing equations consists of the conservative form of the Favre-averaged Navier–Stokes equations plus a transport equation to account for the cavitation dynamics. The equations, written in the Cartesian co-ordinates for the ease of presentation, are presented as follows:

$$\frac{\partial \bar{\rho}_{\mathrm{m}}}{\partial t} + \nabla \cdot (\bar{\rho}_{\mathrm{m}} \tilde{\mathbf{u}}) = 0 \tag{1}$$

$$\frac{\partial (\bar{\rho}_{\mathrm{m}} \tilde{\mathbf{u}})}{\partial t} + \nabla \cdot (\bar{\rho}_{\mathrm{m}} \tilde{\mathbf{u}} \tilde{\mathbf{u}}) = -\nabla \bar{P} + \nabla \cdot (\bar{\tau}_{ij} + \tau_{ij}^{\mathrm{R}}) \tag{2}$$

$$\bar{\tau}_{ij} + \tau_{ij}^{\mathrm{R}} = (\mu + \mu_{\mathrm{t}}) \left[\left(\frac{\partial \tilde{u}_i}{\partial x_j} + \frac{\partial \tilde{u}_j}{\partial x_i} \right) - \frac{2}{3} \delta_{ij} \frac{\partial \tilde{u}_k}{\partial x_k} \right] \tag{3}$$

where P is the pressure, $\mathbf{u}$ the velocity vector, ρ_m the mixture density, μ the laminar viscosity, μ_t the turbulent viscosity, τ_{ij} the viscous stress tensor and τ_{ij}^R the Reynolds stresses based on the Boussinesq's eddy-viscosity hypothesis. The overbar represents a time-average whereas the tilde represents a density-weighted average. Time-derivative terms are dropped for steady flow computations.

For cavitation modelling, a transport equation with source terms is solved:

$$\frac{\partial \bar{\alpha}_L}{\partial t} + \nabla \cdot (\bar{\alpha}_L \tilde{\mathbf{u}}) = \dot{m}^- + \dot{m}^+ \tag{4}$$

where α_L is the liquid volume fraction, $\dot{m}^-$ the source term for evaporation and $\dot{m}^+$ the source term for condensation. The mixture density is defined as

$$\bar{\rho}_m = \rho_L \bar{\alpha}_L + \rho_V (1 - \bar{\alpha}_L) \tag{5}$$

where ρ_L and ρ_V are the liquid and vapour densities, respectively. A nominal density ratio of 1000 is assigned. The particular form of the cavitation models are documented in the next section. For turbulence closure, the original k–ε model with the wall functions is adopted [17, 18].

The present Navier–Stokes solver employs a pressure-based algorithm along with the finite volume approach. The governing equations are solved on multi-block, structured curvilinear grid [19, 20]. The resulting system of equations for turbulent cavitating flows is solved using the pressure-based method developed by Senocak and Shyy [9]. A key feature of this method is to reformulate the pressure correction equation into a convective–diffusive, instead of a pure diffusive, equation. This modification is achieved through the inclusion of a pressure–velocity–density coupling scheme into the pressure-correction equation. For details of the numerical method for turbulent cavitating flows, the reader is referred to Senocak and Shyy [9]. In Part-2 of the present study, we extend the PISO algorithm [21] for turbulent cavitating flows and adopt it in time-dependent computations.

3. TRANSPORT EQUATION-BASED EMPIRICAL CAVITATION MODELS

Three cavitation models adopted in the literature are considered. Each model introduces two empirical parameters. These parameters are typically determined through numerical experimentation. The same parameters can be used for different geometries and flow conditions provided that they are non-dimensionalized with the free stream values [15, 16].

3.1. Model-1 (from References [3, 22])

Several researchers have adopted this model [3, 6, 22]. Both volume and mass fractions have been adopted. Both evaporation and condensation terms are functions of pressure. The liquid volume fraction form is considered in this study

$$\frac{\partial \bar{\alpha}_L}{\partial t} + \nabla \cdot (\bar{\alpha}_L \tilde{\mathbf{u}}) = \frac{C_{dest} \rho_L \, \mathrm{MIN}(\bar{P} - P_V, 0) \bar{\alpha}_L}{\rho_V (0.50 \rho_L U_\infty^2) t_\infty} + \frac{C_{prod} \, \mathrm{MAX}(\bar{P} - P_V, 0)(1 - \bar{\alpha}_L)}{(0.50 \rho_L U_\infty^2) t_\infty} \tag{6}$$

where C_{dest} and C_{prod} are empirical parameters regulating the rate of condensation and evaporation, respectively, U_∞ is the free stream velocity, $t_\infty = L_{ch}/U_\infty$ is the characteristic time scale and L_{ch} is the characteristic length of the flow problem. The subscripts L and V stand for liquid and vapour phases, respectively. The empirical factors adopted in this study have the following values ($C_{\mathrm{dest}} = 1.0,\ C_{\mathrm{prod}} = 8.0 \times 10^1$).

3.2. Model-2 (from Reference [5]*)*

In this model, the liquid volume fraction is chosen as the dependent variable in the transport equation. The evaporation term is a function of pressure whereas the condensation is a function of the volume fraction:

$$\frac{\partial \bar{\alpha}_{\mathrm{L}}}{\partial t} + \nabla \cdot (\bar{\alpha}_{\mathrm{L}} \tilde{\mathbf{u}}) = \frac{C_{\mathrm{dest}} \rho_{\mathrm{V}}\, \mathrm{MIN}(\bar{P} - P_{\mathrm{V}}, 0) \bar{\alpha}_{\mathrm{L}}}{(0.50 \rho_{\mathrm{L}} U_\infty^2) \rho_{\mathrm{L}} t_\infty} + \frac{C_{\mathrm{prod}} \alpha_{\mathrm{L}}^2 (1 - \bar{\alpha}_{\mathrm{L}})}{\rho_{\mathrm{L}} t_\infty} \tag{7}$$

The empirical factors have the following values, ($C_{\mathrm{dest}} = 9.0 \times 10^5,\ C_{\mathrm{prod}} = 3.0 \times 10^4$), as determined previously [9].

3.3. Model-3 (from Reference [23]*)*

In this model, the vapour mass fraction is the dependent variable in the transport equation. Both evaporation and condensation terms are functions of pressure. The model equations adopted here are slightly different from the ones in the original paper [23], which considers non-condensable gas and uses the square root of the turbulent kinetic energy as the characteristic velocity. In our formulation, we use the mean velocity (U_∞) as the characteristic velocity and the non-condensable gas content of the liquid phase is not considered, because cavitation is modelled as a mass transfer process based on the cavitation inception condition ($P < P_{\mathrm{vap}}$).

$$\frac{\partial (\bar{\rho}_{\mathrm{m}} \bar{f}_{\mathrm{V}})}{\partial t} + \nabla \cdot (\bar{\rho}_{\mathrm{m}} \bar{f}_{\mathrm{V}} \tilde{\mathbf{u}}) = (\dot{m}^- + \dot{m}^+) \tag{8}$$

$$\begin{aligned} \dot{m}^- &= C_{\mathrm{dest}} \frac{U_\infty}{\gamma} \rho_{\mathrm{L}} \rho_{\mathrm{V}} (1 - \bar{f}_{\mathrm{V}}) \left[\frac{2}{3} \frac{P_{\mathrm{V}} - \bar{P}}{\rho_{\mathrm{L}}} \right]^{1/2} \quad \text{if } P < P_{\mathrm{V}} \\ \dot{m}^+ &= C_{\mathrm{prod}} \frac{U_\infty}{\gamma} \rho_{\mathrm{L}} \rho_{\mathrm{V}} \bar{f}_{\mathrm{V}} \left[\frac{2}{3} \frac{\bar{P} - P_{\mathrm{V}}}{\rho_{\mathrm{L}}} \right]^{1/2} \quad \text{if } P > P_{\mathrm{V}} \end{aligned} \tag{9}$$

$$\frac{1}{\bar{\rho}_{\mathrm{m}}} = \frac{\bar{f}_{\mathrm{V}}}{\rho_{\mathrm{V}}} + \frac{(1 - \bar{f}_{\mathrm{V}})}{\rho_{\mathrm{L}}} \tag{10}$$

where $\bar{f}$ is the mass fraction and γ is the surface tension. The empirical factors have the following values, ($C_{\mathrm{dest}}/\gamma = 1.225 \times 10^3,\ C_{\mathrm{prod}}/\gamma = 3.675 \times 10^3$).

4. DEVELOPMENT OF AN INTERFACIAL DYNAMICS-BASED CAVITATION MODEL

The development of the model starts by considering a liquid–vapour interface. The mass and normal momentum conservation at such an interface can be written as follows [24]:

$$\rho_{\mathrm{L}}(V_{\mathrm{L},n} - V_{\mathrm{I},n}) = \rho_{\mathrm{V}}(V_{\mathrm{V},n} - V_{\mathrm{I},n}) \tag{11}$$

$$P_{\mathrm{V}} - P_{\mathrm{L}} = \gamma\left(\frac{1}{R_1} + \frac{1}{R_2}\right) + 2\mu_{\mathrm{V}}\frac{\partial V_{\mathrm{V},n}}{\partial n} - 2\mu_{\mathrm{L}}\frac{\partial V_{\mathrm{L},n}}{\partial n} + \rho_{\mathrm{L}}(V_{\mathrm{L},n} - V_{\mathrm{I},n})^2 - \rho_{\mathrm{V}}(V_{\mathrm{V},n} - V_{\mathrm{I},n})^2 \tag{12}$$

where V is the velocity, P the pressure, R the radius of curvature, n the normal direction to the interface, ρ the density, γ the surface tension and μ the viscosity. The subscripts I, L, V represent the interface, the liquid phase and the vapour phase, respectively. Note that the conservation of energy principle is not taken into account because the thermal consideration is excluded. In many practical applications, the physics of the cavitating flow is governed by the hydrodynamics [1, 2] with little thermal implications. On the other hand, in cryogenic applications, the energy conservation principle should also be taken into account.

Figure 1 illustrates a typical liquid–vapour interface based on the homogeneous flow theory. The mixture density is defined as follows based on the liquid volume fraction [25]:

$$\rho_{\mathrm{m}} = \rho_{\mathrm{L}}\alpha_{\mathrm{L}} + \rho_{\mathrm{V}}(1 - \alpha_{\mathrm{L}}) \tag{13}$$

As shown in Figure 1, a hypothetical interface is assumed to lie in the liquid–vapour mixture region. One can further assume that the phase change takes place between the vapour and mixture phases, because in the sharp interface limit, Equation (13) can represents either the vapour or liquid density. In the present formulation, the liquid phase is represented by the mixture phase and hence, the mass and normal momentum conservation reduces to the following forms after dropping the viscous and surface tension effects because of their negligible

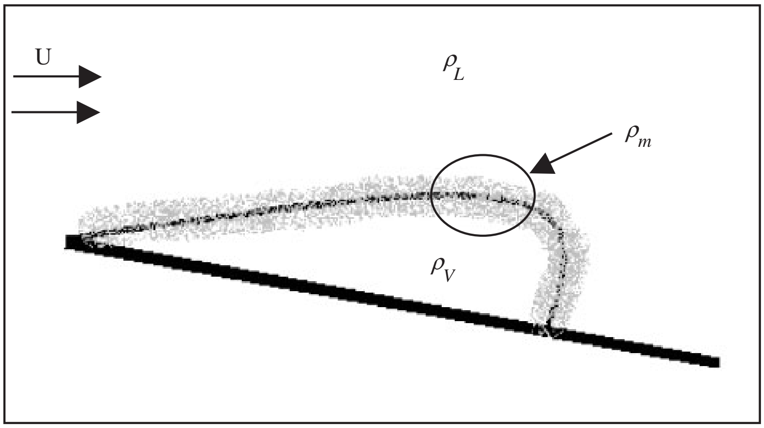

Figure 1. Representation of a vapourous cavity in homogeneous flow theory.

contributions for flows at high Reynolds numbers (e.g. above 10^5)

$$\rho_{\mathrm{V}}(V_{\mathrm{V},n} - V_{\mathrm{I},n}) = \rho_{\mathrm{m}}(V_{\mathrm{m},n} - V_{\mathrm{I},n}) \tag{14}$$

$$P_{\mathrm{V}} - P_{\mathrm{L}} = \rho_{\mathrm{m}}(V_{\mathrm{m},n} - V_{\mathrm{I},n})^2 - \rho_{\mathrm{V}}(V_{\mathrm{V},n} - V_{\mathrm{I},n})^2 \tag{15}$$

From the mass conservation condition, Equation (14), the following relation can be deduced:

$$(V_{\mathrm{m},n} - V_{\mathrm{I},n}) = \frac{\rho_{\mathrm{V}}(V_{\mathrm{V},n} - V_{\mathrm{I},n})}{\rho_{\mathrm{m}}} \tag{16}$$

The momentum conservation condition, Equation (15), can be rearranged by incorporating the mass conservation condition, Equations (14), and (16), resulting in the following form:

$$P_{\mathrm{V}} - P_{\mathrm{L}} = \rho_{\mathrm{V}}(V_{\mathrm{V},n} - V_{\mathrm{I},n})^2 \cdot \left(\frac{\rho_{\mathrm{V}}}{\rho_{\mathrm{m}}} - 1\right) \tag{17}$$

At this point, the definition of the mixture density, given in Equation (13), is incorporated into the above equation that leads to the following forms:

$$P_{\mathrm{V}} - P_{\mathrm{L}} = \rho_{\mathrm{V}}(V_{\mathrm{V},n} - V_{\mathrm{I},n})^2 \cdot \left(\frac{\rho_{\mathrm{V}}}{\rho_{\mathrm{L}}\alpha_{\mathrm{L}} + \rho_{\mathrm{V}}(1-\alpha_{\mathrm{L}})} - 1\right) \tag{18}$$

$$(\rho_{\mathrm{V}} - \rho_{\mathrm{L}})\alpha_{\mathrm{L}} = \frac{(P_{\mathrm{V}} - P_{\mathrm{L}})\rho_{\mathrm{L}}\alpha_{\mathrm{L}} + (P_{\mathrm{V}} - P_{\mathrm{L}})\rho_{\mathrm{V}}(1-\alpha_{\mathrm{L}})}{\rho_{\mathrm{V}}(V_{\mathrm{V},n} - V_{\mathrm{I},n})^2} \tag{19}$$

The final form defining the liquid volume fraction after further arrangement becomes

$$\alpha_{\mathrm{L}} = \frac{\rho_{\mathrm{L}}(P_{\mathrm{L}} - P_{\mathrm{V}})\alpha_{\mathrm{L}}}{\rho_{\mathrm{V}}(V_{\mathrm{V},n} - V_{\mathrm{I},n})^2(\rho_{\mathrm{L}} - \rho_{\mathrm{V}})} + \frac{(P_{\mathrm{L}} - P_{\mathrm{V}})(1-\alpha_{\mathrm{L}})}{(V_{\mathrm{V},n} - V_{\mathrm{I},n})^2(\rho_{\mathrm{L}} - \rho_{\mathrm{V}})} \tag{20}$$

In the context of the TEM, one can couple the above interfacial condition as a source term into the transport equation of liquid volume fraction, based on a dimensional argument. Such practices are often adopted in turbulence modelling [26]. Equation (20) is normalized with a characteristic time scale, defined as $t_\infty = L_{\mathrm{ch}}/U_\infty$. The time scale is chosen based on the characteristics length scale and the free stream velocity to be consistent with the Reynolds number definition. With this choice of the time scale, the source terms represent the mass transfer rates of the bubble cluster, but not the mass transfer rates of single bubbles. The rate of generation of α_{L} is then written as

$$\dot{S} = \frac{\alpha_{\mathrm{L}}}{t_\infty} = \underbrace{\frac{\rho_{\mathrm{L}}(P_{\mathrm{L}} - P_{\mathrm{V}})\alpha_{\mathrm{L}}}{\rho_{\mathrm{V}}(V_{\mathrm{V},n} - V_{\mathrm{I},n})^2(\rho_{\mathrm{L}} - \rho_{\mathrm{V}})t_\infty}}_{\mathrm{I}} + \underbrace{\frac{(P_{\mathrm{L}} - P_{\mathrm{V}})(1-\alpha_{\mathrm{L}})}{(V_{\mathrm{V},n} - V_{\mathrm{I},n})^2(\rho_{\mathrm{L}} - \rho_{\mathrm{V}})t_\infty}}_{\mathrm{II}} \tag{21}$$

The above source term coupled to the transport equation of α_{L} is shown below:

$$\frac{\partial\alpha_{\mathrm{L}}}{\partial t} + \nabla\cdot(\alpha_{\mathrm{L}}\mathbf{u}) = \frac{\rho_{\mathrm{L}}(P_{\mathrm{L}} - P_{\mathrm{V}})\alpha_{\mathrm{L}}}{\rho_{\mathrm{V}}(V_{\mathrm{V},n} - V_{\mathrm{I},n})^2(\rho_{\mathrm{L}} - \rho_{\mathrm{V}})t_\infty} + \frac{(P_{\mathrm{L}} - P_{\mathrm{V}})(1-\alpha_{\mathrm{L}})}{(V_{\mathrm{V},n} - V_{\mathrm{I},n})^2(\rho_{\mathrm{L}} - \rho_{\mathrm{V}})t_\infty} \tag{22}$$

The first term on the right-hand side, compared to the second term, is scaled naturally by a factor of the nominal density ratio (ρ_L/ρ_V). To utilize the above equation, the vapour phase velocity normal to the interface ($V_{V,n}$) and the velocity of the interface ($V_{I,n}$) are needed.

The derivation of the model is based on an existing interface; hence, conditional statements are required on the pressure terms in order to couple the model to the flow computation. The cavitation inception occurs once the hydrodynamic pressure drops below the thermodynamic vapour–pressure value of the corresponding liquid [2]. As seen from Equation (21), in the pure liquid phase ($\alpha_L = 1$) the second term is zero and only the first term can respond to a pressure drop below the thermodynamic vapour–pressure value. Hence, the inception condition is imposed as a minimum (MIN) function Equation (21). Similarly, in the pure vapour phase ($\alpha_L = 0$) the first term is zero and only the second term can respond to a pressure increase above the thermodynamic vapour–pressure value. Hence, the designated condensation condition is imposed as a maximum (MAX) function on the pressure difference term of the second term. In short, the first term of Equation (21) is responsible for conversion from liquid phase back to vapour phase (*evaporation*), and the second term of Equation (21) is responsible for conversion from vapour phase back to liquid phase (*condensation*). With these inclusions, the model equation to be solved along with Favre-averaged Navier–Stokes equations is the following:

$$\frac{\partial \bar{\alpha}_L}{\partial t} + \nabla \cdot (\bar{\alpha}_L \tilde{\mathbf{u}}) = \frac{\rho_L \, \mathrm{MIN}(\bar{P} - P_V, 0)\bar{\alpha}_L}{\rho_V (V_{V,n} - V_{I,n})^2 (\rho_L - \rho_V) t_\infty} + \frac{\mathrm{MAX}(\bar{P} - P_V, 0)(1 - \bar{\alpha}_L)}{(V_{V,n} - V_{I,n})^2 (\rho_L - \rho_V) t_\infty} \tag{23}$$

With the above interfacial dynamics argument, Equation (23) forms a transport equation-based cavitation model for Navier–Stokes computations of cavitating flows. Furthermore, the present model has similar terms as Model-1 [3, 22], but the empirical factors can now be interpreted by the following physical terms:

$$\frac{C_{\mathrm{dest}}}{0.50 \rho_L U_\infty^2} \rightarrow \frac{1}{(\rho_L - \rho_V)(V_{V,n} - V_{I,n})^2}, \quad \frac{C_{\mathrm{prod}}}{0.50 \rho_L U_\infty^2} \rightarrow \frac{1}{(\rho_L - \rho_V)(V_{V,n} - V_{I,n})^2} \tag{24}$$

The model requires that an interface be constructed in order to compute the interface velocity ($V_{I,n}$), as well as the normal velocity of the vapour phase. However, in steady-flow computation, the interface velocity ($V_{I,n}$) is zero and the normal direction of the vapourous cavity can be computed by taking the gradient of the phase volume fraction [27, 28]. Owing to the single fluid formulation, **u** represents the liquid velocity in the liquid phase and the vapour velocity in the vapour phase. Hence, the vapour phase normal velocity is the dot product of the velocity and the normal vector:

$$\mathbf{n} = \frac{\nabla \bar{\alpha}_L}{|\nabla \bar{\alpha}_L|} \quad V_{V,n} = \tilde{\mathbf{u}} \cdot \mathbf{n} \tag{25}$$

The derivatives with respect to curvilinear co-ordinates are computed using central differencing of the neighbouring cell-centred nodes. Senocak [13] has provided the details.

Since the interfacial velocities appear in the denominator of the source terms, there is a possibility of division by zero or by very small numbers, which can arise while computing the normal vectors of the interface at sharp locations. To avoid encountering this situation, a filter is devised to smooth out the interfacial terms. In the filtering process, first, a cutoff is applied on the interfacial term and then interfacial term at a node is updated by the average of the surrounding nodes.

5. RESULTS AND DISCUSSION

Three flow configurations are considered, namely, (i) an axisymmetric cylindrical object with a hemispherical forehead (referred to as hemispherical object) at a Reynolds number of 1.36×10^5, (ii) the NACA66MOD hydrofoil at an angle of attack of 4° with a Reynolds number of 2.0×10^6 and (iii) a convergent–divergent nozzle at a Reynolds number of 2.0×10^6. It is experimentally observed that sheet (attached) cavitation occurs in a quasi-steady fashion for all three of the geometries under the given conditions and only time-averaged experimental data of pressure distribution along the surface are available for hemispherical object [29] and the NACA66MOD hydrofoil [30]. In their experimental study, Stutz and Reboud [31] have detailed the two-phase flow structure of the stable sheet cavitation in a convergent–divergent nozzle and have provided time-averaged velocity and vapour volume fraction profiles within the attached cavity. In this part of the study, only steady flow computations are performed.

5.1. Flow over a hemispherical object

Figure 2 compares the performance of the various cavitation models for the hemispherical object at a cavitation number of 0.30. A grid sensitivity study has been previously reported for

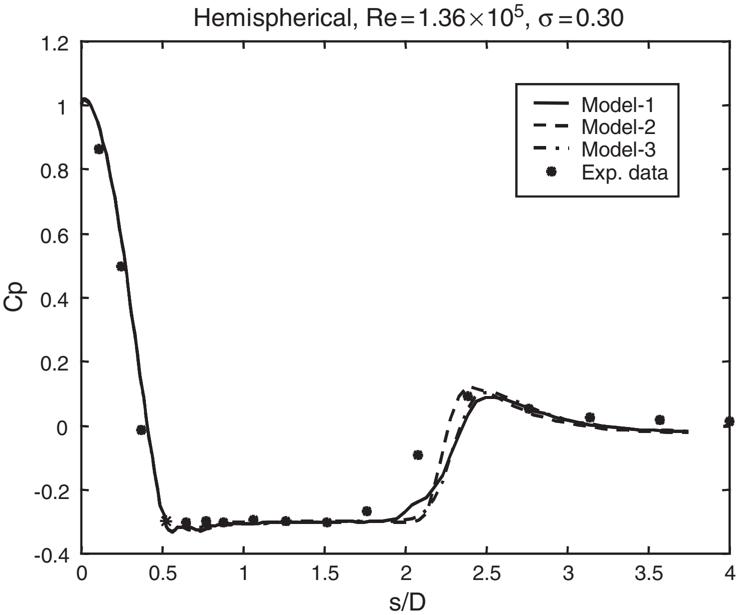

Figure 2. Comparison of surface pressure distribution obtained from empirical cavitation models. Experimental data is from Reference [29].

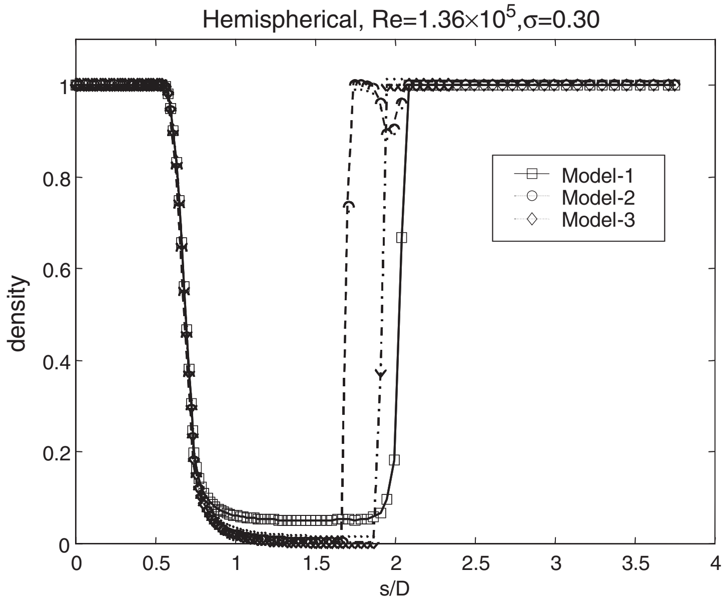

Figure 3. Comparison of surface density distribution obtained from empirical cavitation models.

this particular case in Senocak and Shyy [9]. It has been shown that the pressure and density are not sensitive to the range of grid resolution investigated. The 2D computation is based on a single block body-fitted curvilinear grid with 7.8×10^3 nodes. As shown in Figure 2, all three empirical cavitation models match the experimental pressure distribution satisfactorily. Differences in model performance are more noticeable in the closure region, where the vapour phase condenses. Figure 3 shows the corresponding density distribution along the surface. As seen from density plots, the liquid phase first expands and vapour phase appears uniformly inside the cavity, then the vapour phase compresses, in a sharp rate, back to the liquid phase. High density ratios, close to 1000, are attained by the present numerical method without computational instability. However, noticeable differences are observed among the three models in density profiles, indicating that the cavitation models generate different compressibility characteristics. This issue has important implications in time-dependent problems, and will be investigated in Part-2 of the present study [32].

In Figure 4, the performance of the new interfacial dynamics cavitation model is assessed through comparison with its empirical counter part, Model-1 [3, 22]. Similar to what is observed in Figure 2, the prediction of pressure remains insensitive to the cavitation model choice. A noticeable difference exists in density distribution within the cavity. The density ratio is higher in the new model prediction, close to 1000. Plate 1 shows the distribution of density throughout the cavity and the spanwise vorticity distribution obtained from all four cavitation models. The interface is captured more sharply with the new interfacial dynamics model, Model-2 [5] and Model-3 [23] than with Model-1 [3, 22], especially in the downstream region of the cavity. As seen from the spanwise vorticity distribution, also given in Plate 1, all models capture the additional generation of vorticity in the closure region.

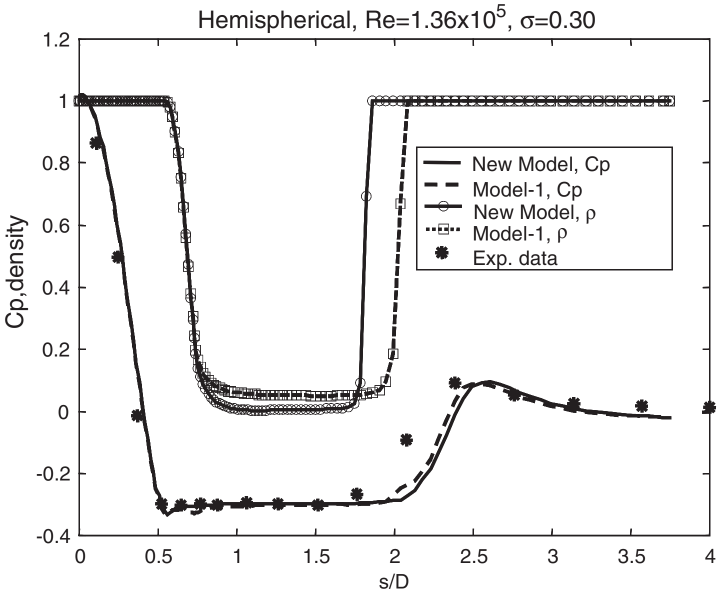

Figure 4. Comparison of surface pressure and density distribution obtained from empirical Model-1 and the new interfacial dynamics model. Experimental data is from Reference [29].

5.2. Flow over an NACA66MOD hydrofoil

The NACA66MOD hydrofoil flow is computed at a Reynolds number of 2×10^6. The turbulent boundary layer is extremely thin at such a high Reynolds number. Since the original k–ε turbulence model along with the wall function is adopted, it is important to offer spatial resolutions consistent with the modelling requirement [33]. This requires that the non-dimensional normal distance from the wall (y^+), a representation of the local Reynolds number, should be in the log-law region. Once a cavity occurs on the surface, the local Reynolds number decreases due to reduction in density and the first grid point away from the wall may not be positioned in the log layer, but it can be within the viscous sublayer. This issue has important implications in both accuracy and numerical stability. It is found that proper grid distribution is critical for such computations. However, there is a trade-off between positioning the first grid point away from the wall in the log layer, required by the wall function formulation, verses having enough points to discretize the cavity, especially for high Reynolds number cases. To illustrate the issues involved, two two-dimensional grids have been tested. Model-2 [5] is used in the computations as the cavitation closure. Grid-A is a three-block grid with approximately 2.2×10^4 nodes, whereas Grid-B is a six-block grid with approximately 3.3×10^4 nodes. Close-up views of the same region in both grids are shown in Figure 5 to demonstrate the differences in spatial resolution. The boundary of the cavitating region is also highlighted on the grids to give an idea of how many grid points are available to discretize the vapour cavity. Note that the first grid point in Grid-B is positioned to satisfy the (y^+) requirement and the rest of the points are clustered close to it. In Figure 6, the y^+ distribution of the first grid points away from the wall is plotted along the surface. The law of the wall is also highlighted on this plot.

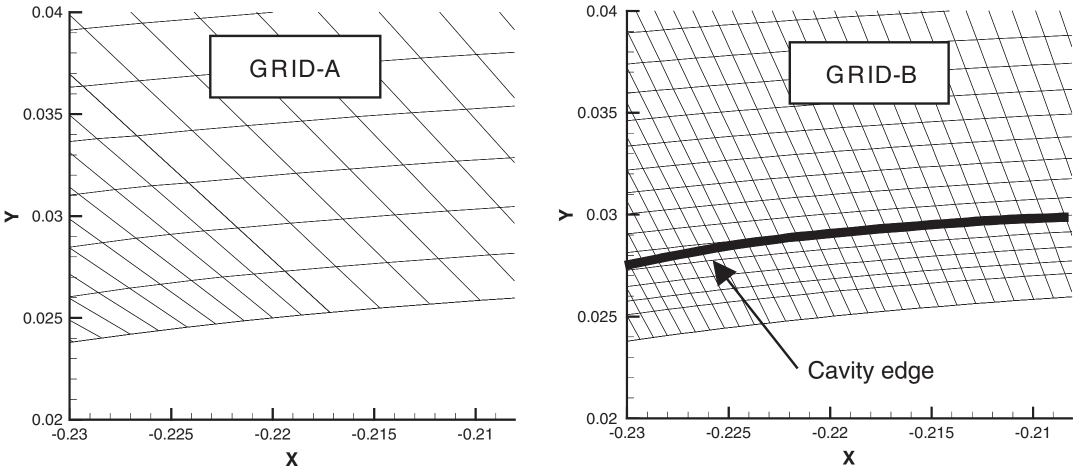

Figure 5. Visual comparison of the grid distributions.

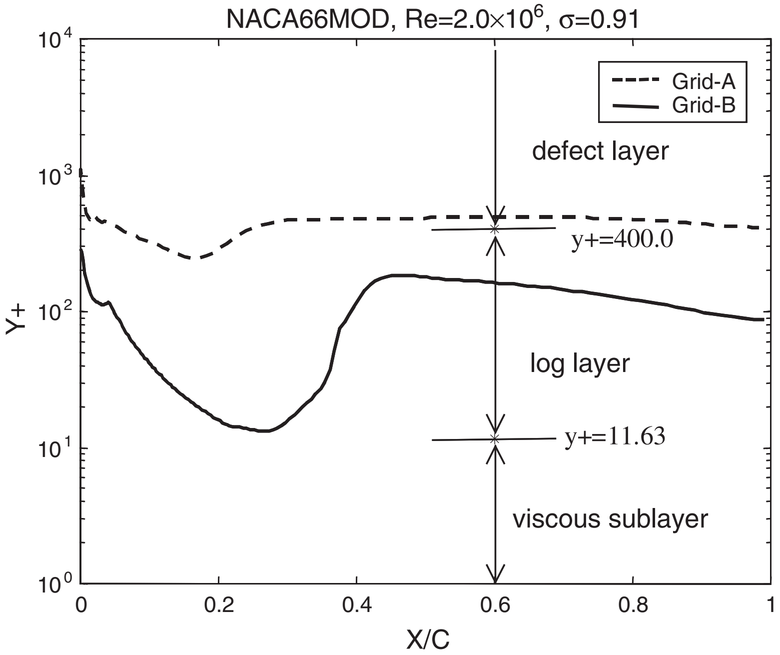

Figure 6. Distribution of the y^+ values of the first grid points away from the wall along the hydrofoil surface.

As shown in Figure 7, the predictions with Grid-A are poor compared to the case with Grid-B. A very short cavity has been captured with Grid-A as a result of inadequate spatial resolution. The vapour cavity is so thin that Grid-A can only accommodate two grid points in

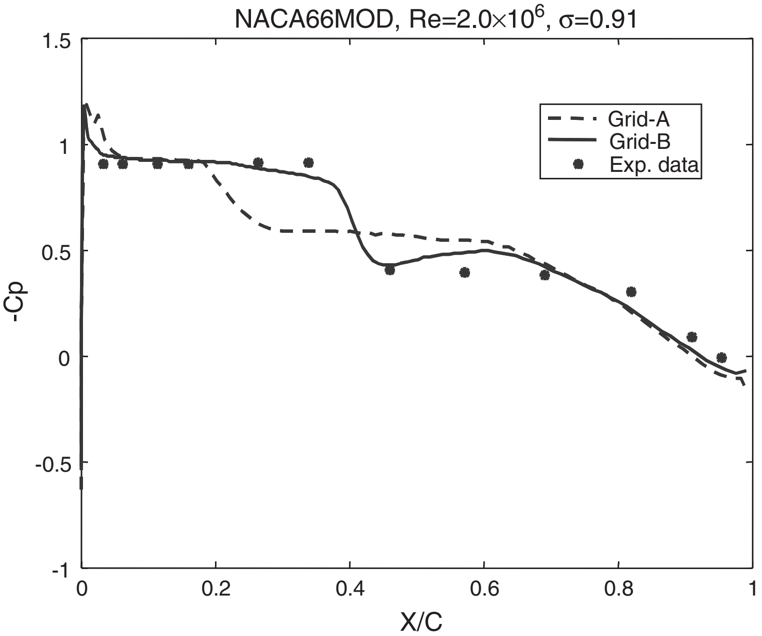

Figure 7. Effect of grid distribution on predictions. Model-2 is used. Experimental data is from Reference [30].

this region. On the other hand, Grid-B, the finer grid, produces results in agreement with the experiments. As can be observed in Figure 5, special attention has been given to place the points of the Grid-B in the log layer. A higher resolution grid is also utilized and it is found that if the y^+ values of the cavitating region are in the viscous sublayer, the computation is not stable. This may be because in the wall function formulation a linear velocity profile is imposed in the viscous sublayer and such a profile may not be suitable to represent the phase change dynamics. It should be emphasized that the original k–ε turbulence model is based on the equilibrium assumption, and the rate of turbulence production and dissipation are balanced in the log-layer; hence, it is advisable to place the near wall region in the log layer [34]. If higher resolution is required, a low Reynolds number two-equation turbulence model should be the choice. Nevertheless, Grid-B is used for all other computations of NACA66MOD hydrofoil case and the original k–ε model with the wall functions is adopted for turbulence closure.

In Figures 8 and 9, the performance of the cavitation models has been assessed for cavitation numbers of 0.91 and 0.84, respectively. For cavitation number of 0.84, the vapourous cavity covers about 60% of the hydrofoil surface. All three empirical cavitation models and the new interfacial dynamics cavitation model produce satisfactory results at both cavitation numbers. Differences in predictions are more pronounced, similar to the hemispherical object case, at the closure region, which is due to the different compressibility characteristics imposed by the cavitation models.

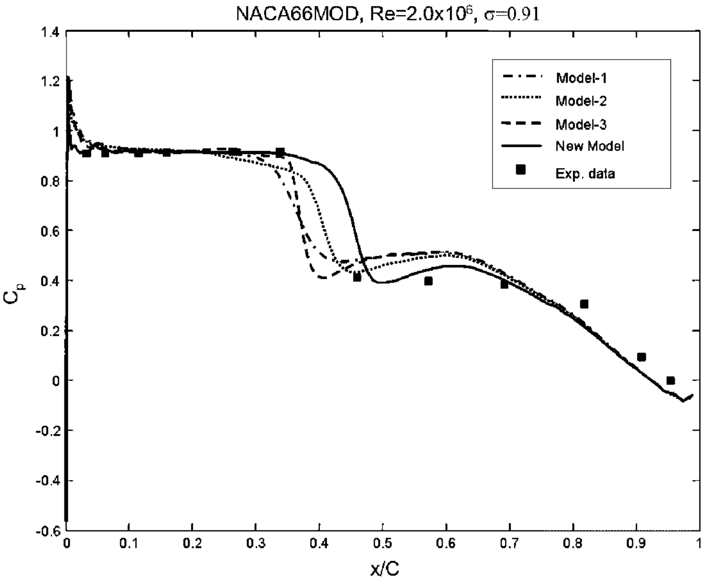

Figure 8. Comparison of surface pressure distribution. The cavitation number is 0.91. Experimental data is from Reference [30].

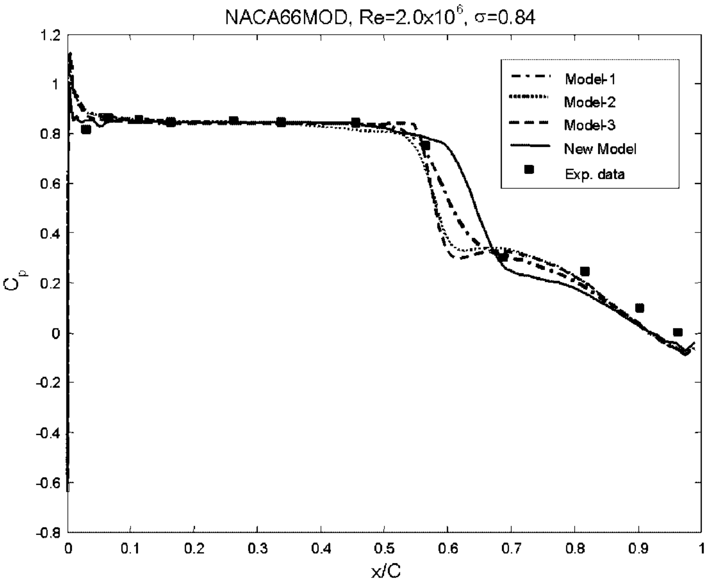

Figure 9. Comparison of surface pressure distribution. The cavitation number is 0.84. Experimental data is from Reference [30].

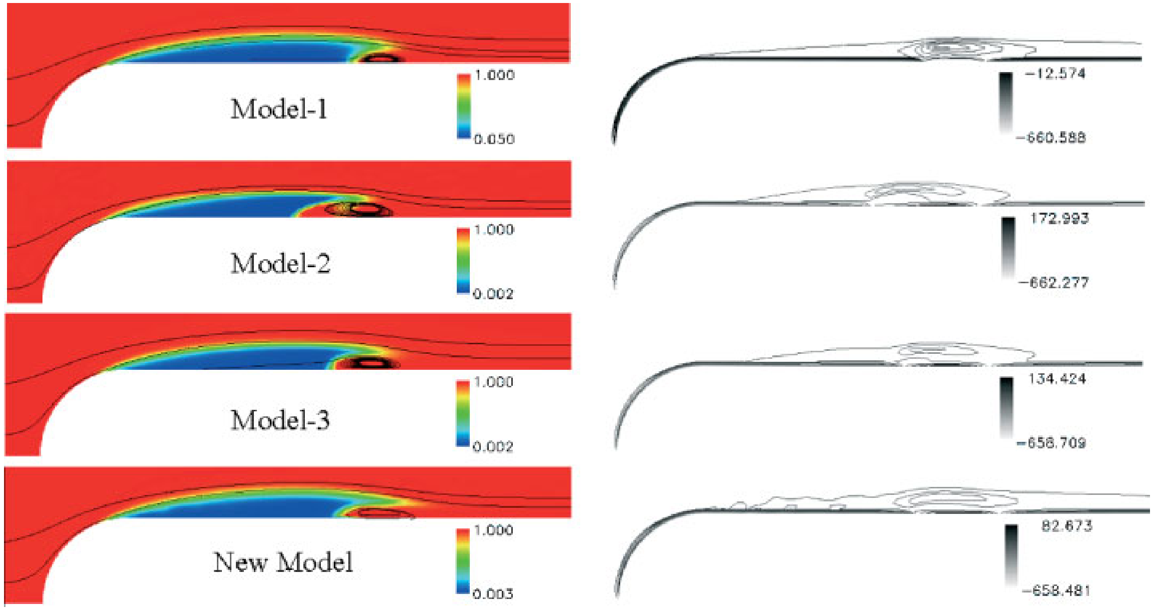

Plate 1. Detailed view of the cavitating region. On the left is the density distribution; on the right is the spanwise vorticity distribution.

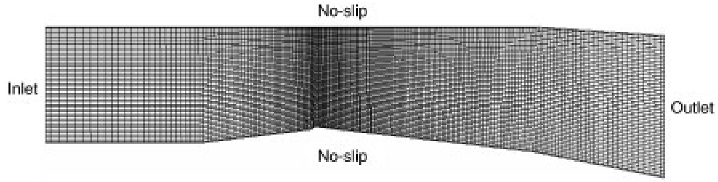

Figure 10. The computational domain and the imposed boundary conditions for the convergent–divergent nozzle.

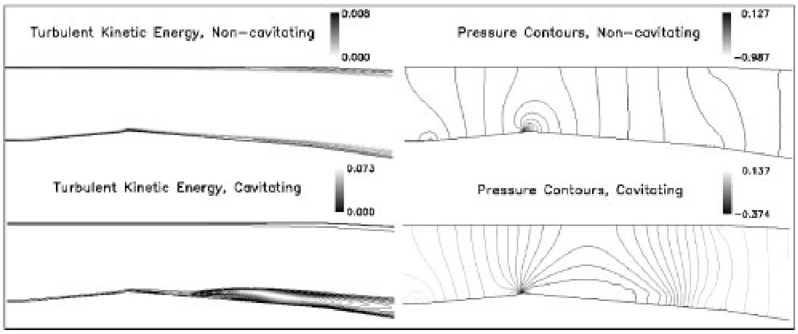

Figure 11. The impact of cavitation on the structure of internal flow through the nozzle.

5.3. Convergent–divergent nozzle (Stable sheet cavitation)

Stutz and Reboud [31] have conducted experiments to detail the flow structure within sheet cavitation. A convergent–divergent nozzle with a venturi-type test section is adopted. The test section is 520 mm long 44 mm wide and 50 mm high at the inlet. The throat height is 43.7 mm. The angle of the convergent part is 4.3°, whereas the divergent section angle is 4.0°. A sharp ridge is formed at the throat section to induce further pressure drop. The experiments have been carried for a cavitation number ranging between 0.60 and 0.75. The Reynolds number ranges from 4.3×10^5 to 2.1×10^6. The accuracy of the velocity measurements is ±10%. The results have been presented for a mean cavity length of 80 mm. The LDA measurements have indicated a nearly 2D flow. Based on this information from Stutz and Reboud [31], the cavitation number and the Reynolds number are chosen as 0.62 and 2.0×10^6, respectively, for the present computations. The computational domain and the imposed boundary conditions are shown in Figure 10.

Figure 11 shows a comparison between the non-cavitating and cavitating conditions in the nozzle. The turbulent kinetic energy and the pressure fields for both cavitating and non-cavitating conditions are shown. It is clear that cavitation not only alters the local flow details but also the overall flow structure in the nozzle. The highest level of turbulent kinetic energy production is just downstream of the cavity. This finding is in good agreement with the experimental results of Gopalan and Katz [14], who have also studied sheet cavitation in a nozzle but with a different geometry and flow conditions. The pressure field in the throat section is noticeably affected due to the presence of sheet cavitation, also shown in Figure 11.

As can be deduced from the contour plots, the pressure gradient field under cavitating conditions is more complex compared to the non-cavitating conditions. Strong adverse pressure gradients are responsible for the reverse flow in the closure region, which does not exist in non-cavitating conditions. Adverse pressure gradients are known to be responsible for the re-entrant jet cavitation instability [35].

It is important to know the source of turbulence production in the closure region. In particular, this information can be helpful in identifying possible areas of improvement in computational modelling of cavitation. It is well known that the original k–ε model has deficiencies for complex flow structure [26]. Nevertheless, for cavitating flows, there is insufficient information to suggest a more complicated model for realistic geometries and flow parameters. Gopalan and Katz [14] concluded that the origin of the turbulence production is the collapse of the cavities in the closure region, which results in vorticity generation. Obviously, the collapse of the cavities cannot be well simulated within the present steady-state assumptions, but the spanwise vorticity field has indicated additional vorticity in the closure region, as shown previously in the hemispherical object case. Considering the fact that an adverse pressure gradient generates a recirculation zone behind sheet cavitation, the main question to be asked is; what are the effective terms in the vorticity transport equation responsible for the generation of spanwise vorticity in the closure region. The vorticity transport equation is written as [1]

$$\frac{\partial \boldsymbol{\omega}}{\partial t} + \nabla \times (\boldsymbol{\omega} \times \mathbf{u}) = \frac{1}{\rho^2} \nabla \rho \times \nabla P + \upsilon \nabla^2 \boldsymbol{\omega} \tag{26}$$

Figure 12 shows the contour plots of the effective terms of the vorticity transport equation along with the spanwise vorticity distribution. Clearly, the baroclinic term of the vorticity transport equation is important in the closure region of the cavity. Hence, it can be concluded that the additional turbulence production is driven by the baroclinic vorticity generation.

Figure 13 shows a direct comparison of the computed cavity and velocity vectors with the experiment. The results are in good agreement with the experiment and indicate the thickening of the boundary layer in cavitating regions. The boundary layer follows the cavity boundary but slightly thicker than the cavity. The experiments show the reverse flow behind the cavity but it is not presented in this particular plot.

A more direct comparison of the cavity boundary and velocity profiles within cavity is also performed. As seen in Figure 14, the cavity boundary and it is overall shape is reasonably captured by the computations. Discrepancy exists in terms of the quantitative extent of the reverse flow. The present results indicate a shorter one, which results in different velocity profiles. Figure 15 presents the comparison of vapour volume fraction distribution. The experimental data indicate a mixture in the reverse flow whereas the computation captures a pure liquid reverse flow. The vapour content is noticeably higher in the computational results.

The discrepancy observed in velocity and void fraction profiles result in part from the steady flow computations; in Part-2 of the present study [32] we will show that time-dependent simulations can produce a better agreement with the experimental data.

6. CONCLUSIONS

The present study has focused on understanding the relative merits of transport equation-based cavitation models. Favre-averaged Navier–Stokes equations, cast in their conservative form,

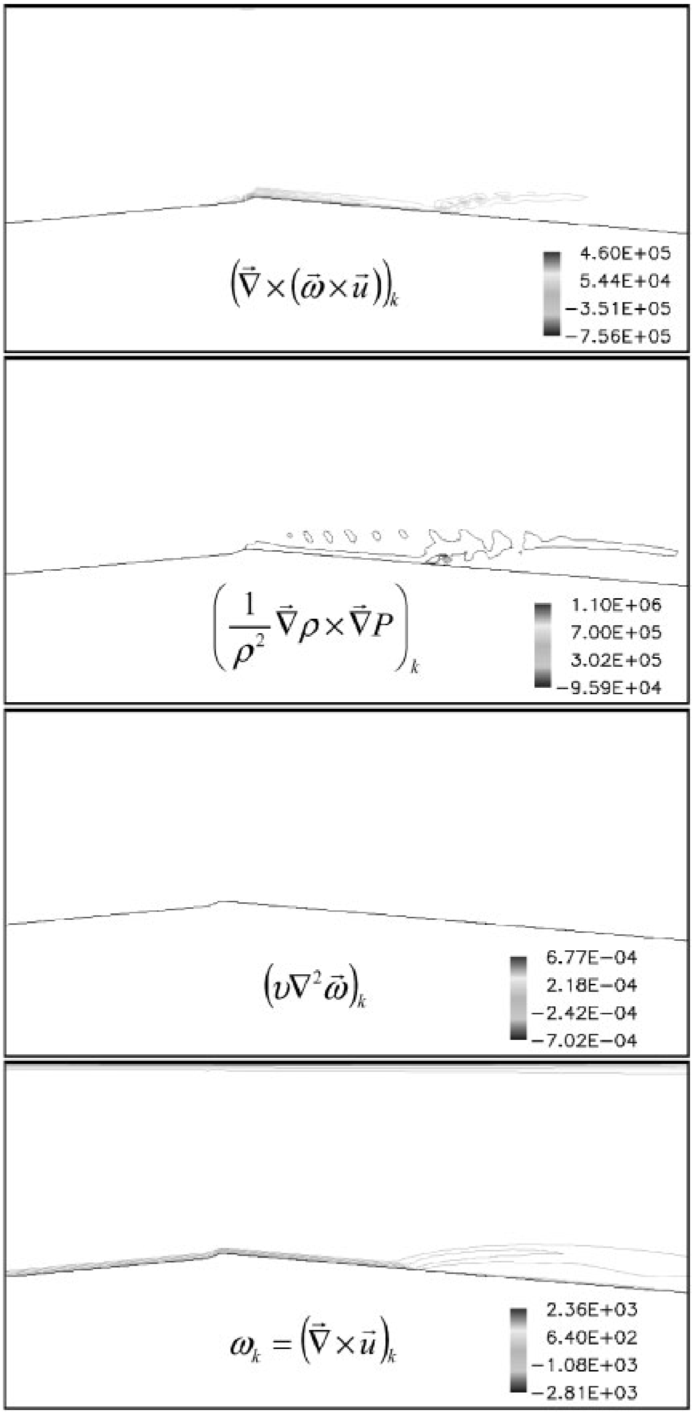

Figure 12. The effective terms of the vorticity transport equation for cavitating conditions.

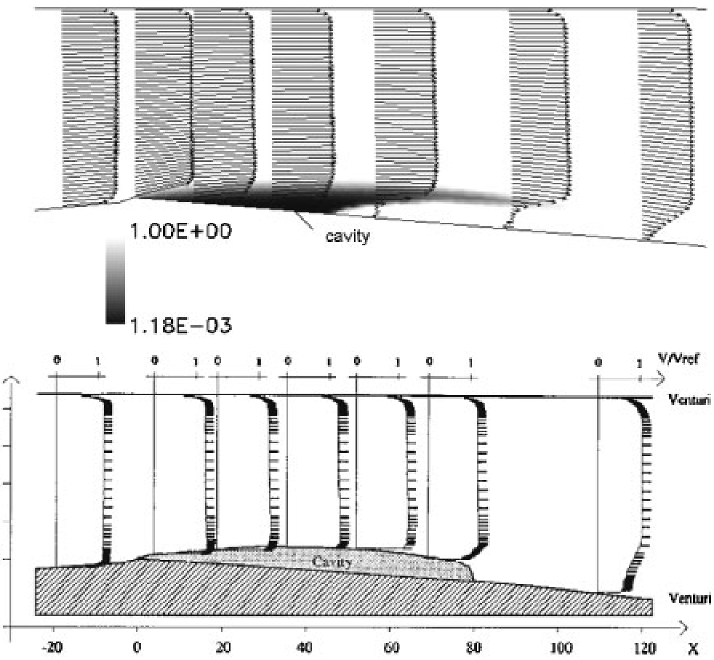

Figure 13. The velocity field around sheet cavitation. The bottom plot is reproduced from the experimental study of Stutz and Reboud [31] with the permission of authors.

along with transport equation-based cavitation models and the original *k*–ε turbulence model have been employed. A unified pressure-based method for turbulent cavitating flows [9] has been adopted for the computations.

Three versions of the transport equation-based empirical cavitation models have been considered. An analysis of the mass and momentum conservation at a liquid–vapour interface has been conducted in the context of homogeneous equilibrium flow theory. The analysis helps shed light into the source of empiricism in the existing transport equation-based cavitation models. Based on the analysis of interfacial dynamics, a new transport equation-based interfacial dynamics cavitation model has been developed.

Three flow configurations have been tested, including a hemispherical projectile, the NACA 66MOD hydrofoil and a convergent–divergent nozzle. The new interfacial dynamics cavitation model and the existing empirical cavitation models considered have produced qualitatively comparable results in wall pressure distributions. However, quantitative differences in pressure and density distributions, especially in the closure region, are observed, implying that the compressibility effects are handled differently in the cavitation models. These differences can significantly impact the time-dependent flow computations. In Part-2 of the present study [32], the issue is investigated in more depth.

The abrupt change of density profiles across the cavity boundary has implications on the near-wall turbulence treatment with the *k*–ε turbulence model. Owing to reduction of density in the cavitating region, the local Reynolds number reduces substantially, which can create difficulty to accommodate the resolution requirement in both liquid and cavity regions. The

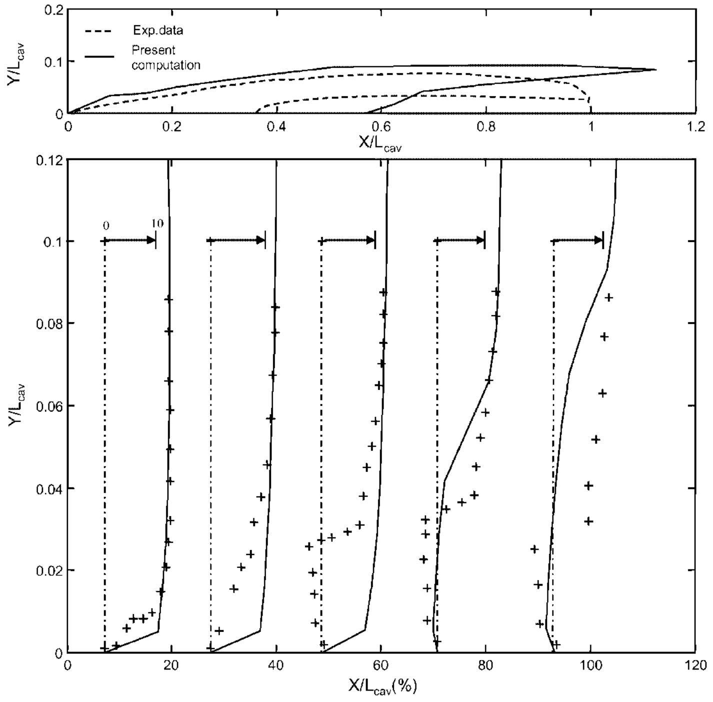

Figure 14. Comparison of the cavity boundary and the velocity profiles within the cavity. Experimental data is from Reference [31].

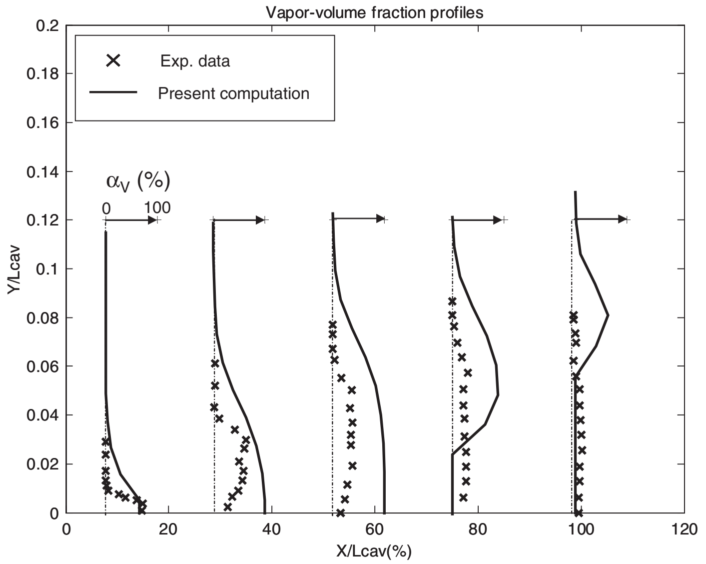

Figure 15. Vapour volume fraction profiles within the cavity. Experimental data is from Reference [31].

issue causes difficulties in numerical stability of cavitating flow computations, if the grid resolution of the cavity includes the viscous sublayer. The problem has been identified and overcome by adopting wall-function consistent grids that resolves the cavity within the log-law region of the turbulent boundary layer.

The new interfacial dynamics cavitation model has been further applied to a convergent–divergent nozzle flow problem to study the two-phase flow structure of sheet cavitation. It is found that the baroclinic term of the vorticity transport equation is effective in the closure region that contributes to the highest level of turbulent kinetic energy production there. The sheet cavitation formed in the nozzle affects the overall flow structure in the nozzle. Strong adverse pressure gradients are responsible for the reverse flow in the closure region, which do not exist for the non-cavitating case. Although steady flow computations yield satisfactory pressure distributions and highlight important flow structures, the velocity and void fraction profiles are not well captured. We will further investigate this issue by adopting time-accurate computations in Part-2 of the present study [32], demonstrating improved predictions.

ACKNOWLEDGEMENTS

This study has been supported partially by the NASA URETI programme and the U.S. Air Force. The first author would like to thank Marianne Francois for helpful discussions on computation of normal velocities. We also appreciate B. Stutz and J. L. Reboud for the interactions regarding their experimental study.

REFERENCES

1. Batchelor GK. *An Introduction to Fluid Dynamics*. Cambridge University Press: New York, 1967.
2. Knapp RT, Daily JW, Hammitt FG. *Cavitation*. McGraw-Hill: New York, 1970.
3. Merkle CL, Feng JZ, Buelow PEO. Computational modeling of the dynamics of sheet cavitation. *Proceedings of the 3rd International Symposium on Cavitation*, Grenoble, France, 1998.
4. Edwards JR, Franklin RK, Liou MS. Low-diffusion flux-splitting methods for real fluid flows with phase transitions. *AIAA Journal* 2000; **38**(9):1624.
5. Kunz RF, Boger DA, Stinebring DR, Chyczewski TS, Lindau JW, Gibeling HJ, Venkateswaran S, Govindan TR. A preconditioned Navier–Stokes method for two-phase flows with application to cavitation prediction. *Computers and Fluids* 2000; **29**:849.
6. Ahuja V, Hosangadi A, Arunajatesan S. Simulations of cavitating flows using hybrid unstructured meshes. *Journal of Fluids Engineering* 2001; **123**:331.
7. Venkateswaran S, Lindau JW, Kunz RF, Merkle CL. Preconditioning algorithms for the computation of multiphase mixture flows. *AIAA 39th Aerospace Sciences Meeting & Exhibit*, AIAA-2001-0125.
8. Patankar SV. *Numerical Heat Transfer and Fluid Flow*. Hemisphere: Washington, DC, 1980.
9. Senocak I, Shyy W. A pressure-based method for turbulent cavitating flow computations. *Journal of Computational Physics* 2002; **176**:363.
10. Wang G, Senocak I, Shyy W, Ikohagi T, Cao S. Dynamics of attached turbulent cavitating flows. *Progress in Aerospace Sciences* 2001; **37**:551.
11. Delannoy Y, Kueny JL. Cavity flow predictions based on the Euler equations. *ASME Cavitation and Multi-Phase Flow Forum*, ASME-FED vol. 98, pp. 153–158, 1990.
12. Song CS, Chen X. Numerical simulation of cavitating flows by single-phase flow approach. *Proceedings of the 3rd International Symposium on Cavitation*, Grenoble, France, 1998.
13. Senocak I. Computational methodology for the simulation of turbulent cavitating flows. *Ph.D. Thesis*, University of Florida, Gainesville, FL, U.S.A., 2002, http://purl.fcla.edu/fcla/etd/UFE1001181.
14. Gopalan S, Katz J. Flow structure and modeling issues in the closure region of attached cavitation. *Physics of Fluids* 2000; **12**(4):895.
15. Senocak I, Shyy W. Numerical simulation of turbulent flows with sheet cavitation. *CAV2001 4th International Symposium on Cavitation*, *Paper No*. CAV2001A7.002, Pasadena, CA, U.S.A., 2001, http://cav2001.library.caltech.edu.

16. Rajkumar V, Senocak I, Wu J, Shyy W. Sensitivity evaluation of a transport-based turbulent cavitation model. *Journal of Fluids Engineering* 2003; **125**(3):447.
17. Jones WP, Launder BE. The prediction of laminarization with a two-equation model of turbulence. *International Journal of Heat and Mass Transfer* 1972; **15**:301.
18. Launder BE, Spalding DB. The numerical computation of turbulent flows. *Computer Methods in Applied Mechanics and Engineering* 1974; **3**:269.
19. Shyy W. *Computational Modeling for Fluid Flow and Interfacial Transport*. Elsevier: Amsterdam, The Netherlands, 1997 (revised printing).
20. Shyy W, Thakur SS, Ouyang H, Liu J, Blosch E. *Computational Techniques for Complex Transport Phenomena*. Cambridge University Press: New York, 1997.
21. Issa RI. Solution of the implicitly discretized fluid flow equations by operator-splitting. *Journal of Computational Physics* 1985; **62**:40.
22. Singhal AK, Vaidya N, Leonard AD. Multi-dimensional simulation of cavitating flows using a PDF model for phase change. *ASME Fluids Engineering Division Summer Meeting*, *ASME Paper* FEDSM97-3272, 1997.
23. Singhal AK, Li NH, Athavale M, Jiang Y. Mathematical basis and validation of the full cavitation model. *ASME Fluids Engineering Division Summer Meeting*, *ASME Paper* FEDSM2001-18015, 2001.
24. Carey VP. *Liquid–Vapour Phase-Change Phenomena*. Hemisphere: Washington, DC, 1992.
25. Wallis GB. *One-dimensional Two-phase Flow*. McGraw-Hill: New York, 1969.
26. Wilcox DC. *Turbulence Modeling for CFD*. DCW Industries, Inc., La Canada, CA, 1993.
27. Brackbill JU, Kothe DB, Zemach C. A continuum method for modeling surface tension. *Journal of Computational Physics* 1992; **100**:335.
28. Francois M. A study of the volume of fluid method for moving boundary problems. *M.Sc. Thesis*, Embry Riddle Aeronautical University, Daytona Beach, FL, U.S.A., 1998.
29. Rouse H, McNown JS. Cavitation and pressure distribution, head forms at zero angle of yaw. *Studies in Engineering*, State University of Iowa, 1948; Bulletin 32.
30. Shen Y, Dimotakis P. The influence of surface cavitation on hydrodynamic forces. *Proceedings of 22nd ATTC*, St. Johns, 1989; 44.
31. Stutz B, Reboud JL. Two-phase flow structure of sheet cavitation. *Physics of Fluids* 1997; **9**(12):3678.
32. Senocak I, Shyy W. Interfacial dynamics-based modeling of turbulent cavitating flows, Part-2: Time-dependent computations. *International Journal for Numerical Methods in Fluids* 2004; **44**:997–1016.
33. He X, Senocak I, Shyy W, Gangadharan SN, Thakur S. Evaluation of laminar-turbulent transition and equilibrium near wall turbulence models. *Numerical Heat Transfer A* 2000; **37**:101.
34. Versteeg HK, Malalasekera W. *An Introduction to Computational Fluid Dynamics*. Longman: London, 1995; 73.
35. Callenaere M, Franc JP, Michel JM, Riondet M. The cavitation instability induced by the development of a re-entrant jet. *Journal of Fluid Mechanics* 2001; **444**:223.